Flight Path Reconstruction and Flight Test of

Four-line Power Kites

R. Borobia[1] and G. Sanchez-Arriaga[2]
Universidad Carlos III de Madrid, Leganés, 28911, Spain

A. Serino[3]
Politecnico di Torino, Torino, 10129, Italy

R. Schmehl [4]
Delft University of Technology, Delft, 2629HS, The Netherlands

We present a flight path reconstruction algorithm designed for tethered systems with application to airborne wind energy generation and based on an extended Kalman filter (EKF). The kite state vector, with position, velocity, Euler angles, and angular velocities, has been extended to include error models for sensors, and stochastically modeled variables describing the aerodynamic force and torque of the kite, tether tension at the four lines, and wind velocity magnitude and heading angle. The observation model of the EKF gathers information from GPS, accelerometers, gyroscopes, magnetometer, load sensors at all the lines, and airspeed. The algorithm has been fed with real data obtained from an experimental setup. In addition to onboard sensors and load cells, the experiments also monitored the control inputs of the kite by measuring with two distance sensors the position of the control bar steered by the pilot. Several flight tests, which included pull-up and lateral-directional steering maneuvers with two kites of different areas, were conducted and used to investigate the performance of the

---

[1] PhD candidate at Universidad Carlos III de Madrid and Aerospace Engineer at Spanish National Institute of Aerospace Technology (INTA)
[2] Ramón y Cajal Research Fellow, Bioengineering and Aerospace Engineering Department, Avda. de la Universidad 30, 28911, Leganés, Madrid, Spain
[3] Aerospace Engineer
[4] Associate Professor at Delft University of Technology, Faculty of Aerospace Engineering, Kluyverweg 1, 2629HS Delft, The Netherlands

1

EKF. The filter provided the estimation of the kite state-space trajectory during the tests. Important information, such as the aerodynamic forces and torques during the flight, were provided by the algorithm. This work is a first step towards aerodynamic parameter identification of kites and tethered drones using flight tests data.

$\boldsymbol{B}$ $\qquad$ = magnetic field, T

$\tilde{d}_{\pm}$ $\qquad$ = distance sensor measurements, m

D_{cb} $\qquad$ = control bar displacement, m

$\boldsymbol{F}_a$ $\qquad$ = aerodynamic force, N

$\tilde{\boldsymbol{f}}_{IMU}$ = specific force, m/s^2

$\boldsymbol{M}_a$ $\qquad$ = aerodynamic torque, Nm

m_k $\qquad$ = kite mass, kg

S $\qquad$ = kite surface, m^2

L_{cb} $\qquad$ = length of the control bar, m

L_{ds} $\qquad$ = depower stopper distance, m

L_l $\qquad$ = lengths of the frontal lines, m

L_{ps} $\qquad$ = power stopper distance, m

L_t $\qquad$ = lengths of the rear lines, m

L_s $\qquad$ = length of the sliding tether, m

$\bar{\boldsymbol{Q}}$ $\qquad$ = process covariance matrix

$\bar{\boldsymbol{R}}$ $\qquad$ = observation covariance matrix

$\bar{\boldsymbol{R}}_{EB}$ = Earth-Body rotation matrix

s_0 $\qquad$ = control bar-to-load cell distance, m

$\boldsymbol{r}$ $\qquad$ = kite position, m

$\boldsymbol{T}$ $\qquad$ = tether tension, N

$\boldsymbol{v}$ $\qquad$ = kite velocity, m/s

w_{cl} $\qquad$ = width of the chicken-loop interface, m

Δp $\qquad$ = differential pressure, Pa

η $\qquad$ = sensor noise

$\boldsymbol{\Upsilon}$ $\qquad$ = euler angles vector, rad

$\boldsymbol{\omega}$ $\qquad$ = kite angular velocity, rad/s

ρ $\qquad$ = air density, kg/m^3

θ $\qquad$ = pitch angle, rad

Θ $\qquad$ = instrument bias

3

ψ $\qquad$ = yaw angle, rad

ϕ $\qquad$ = roll angle, rad

ν $\qquad$ = control bar deflection angle, rad

χ $\qquad$ = Markov state vector

Subscripts and accents

k = kite

K = Kite-frame

E = Earth-frame

$A_\pm$ = Attachment points $A_\pm$

$B_\pm$ = Attachment points $B_\pm$

$\hat{x}$ = Estimated value of x

$\tilde{x}$ = Measured value of x

I. Introduction

The increasing demand for renewable energy is actively driving the search for more efficient methods to harvest energy from the wind. Although conventional horizontal axis wind turbines, play now an important role in the energy economy of many countries, the technology has a substantial environmental impact and particularly for offshore deployment is still relatively expensive. This has triggered the research on airborne wind energy (AWE) systems based on the pioneering work of Miles Loyd [1]. These devices operate at higher altitude than conventional wind turbines, where, due to more steady and stronger winds, more energy is available. The proposed solutions include the so-called ground- and fly-generation systems (see a review of technologies in Ref. [2]). For a ground-generation system, the high tether tension obtained by flying the kite along optimal crosswind trajectories is used to drive a drum with a connected generator on the ground in pumping cycle with alternating reel-out and reel-in [3, 4]. Fly-generation systems produce the electrical power directly on-board by using wind turbines [5]. An example is the Makani's M600 system developed by Makani Power in USA [6].

The design of wind energy systems based on power kites and capable of operating autonomously for extended periods of time is technically challenging. Similarly to unmanned air vehicles (UAVs), several disciplines, such as system state estimation, control, and guidance, are interrelated. The aerodynamic characterization of the kite plays also a central role. However, the flexible nature of the kite structure, the constraints imposed by the tethers, and the lack of accurate aerodynamic

4

data, are rendering the development of these systems difficult. These issues represent challenges to be added to the already complex design of UAVs. For these reasons, the development of accurate mathematical models validated by flight testing is a priority for the AWE community. Several kite flight simulators with different levels of complexity have been developed in the past [4, 7–12]. Naturally, all of them include an aerodynamic model, which basically receives the airspeed of the kite and returns the aerodynamic coefficients that describe the aerodynamic force and torque about the center of mass of the kite. These coefficients, which are also denoted as stability derivatives, play a central role in the stability of the equilibrium of the kite [13, 14], which is of fundamental interest for many kites applications including the generation of energy. Although analyses with computational fluid dynamics codes has been carried out [15, 16], the complex fluid-structure interaction is still an open and active field of research. Wind tunnel experiments for ram-air wings have been also conducted [17].

On the other hand, additionally to numerical and wind tunnel studies, aircraft aerodynamic characterization based on real flight test data has been used profusely by the aerospace industry in the past. This characterization can be approached by both in a one-step or a two-step techniques. One step techniques, such as the maximum likelihood method, estimate both the state variables and the aerodynamic parameters at the same time by an optimization process. This is done by a formulation of the process model which implicitly includes the aerodynamic derivatives, requiring an a-priori knowledge of the structure of the aerodynamic model[18, 19]. Two steps techniques (or estimation-before-modeling[20, 21]) estimate first the time histories of the state variables of the system. Such a time histories, which include the aerodynamic force and moment, are used in the second phase to perform the aerodynamic parameters identification of the system. Since the space state trajectory estimation, the so called flight-path-reconstruction (FPR) [22], is independent of the proposed aerodynamic model structure, a-priori knowledge of the system is not longer needed, and different model structures can be tested afterwards without a reformulation of the problem. For this reason, the solution of the FPR problem is the first step towards the aerodynamic parameters identification for AWE systems. A recent works have tackled this problem for rigid wing AWE pumping systems [23, 24].

Our contribution consists of two main elements. The first one is a portable and low-cost experimental setup for the acquisition of flight data from four-line kites with tether lengths in the order of several tens of meters. Recent works highlighted the important role of this type of experiments in the progress of AWE systems and the difficulties arising in the determination of the airspeed of the kite [25, 26]. The second element is a solution for the kite FPR problem, which incorporates special features of this type of systems such as the constraints imposed by the tethers and their tensions. For configurations with relatively short lines, tether sagging can be neglected and the accuracy of the GPS can be improved by the geometric constraint introduced by the lines [27, 28].

The work is organized as follows. Section II describes the main elements of the experimental setup and justifies the hardware selection. Two different four-line power kites have been used as platforms and a set of measurement instruments provided state variables, such as position, velocity, acceleration, attitude, angular acceleration, airspeed, and tether tension. Control variables, i.e. the position of the control bar, are also measured during the flight tests. Two key features of the setup are the low cost and portability because it can be easily adapted to other types of kites. An outline of the FPR algorithm is given in Sec. III with full description in Appendix. The experimental results and the performance of the FPR method are given in Sec. IV while the conclusions and applications of the work are presented in Sec. V

II.   Experimental Setup

A.   System layout

Figure 1 shows a schematic of the experimental setup. It involves a 4-line power kite of mass m_k and surface S_k attached to a fixed point O_E on the ground. Such point is the origin of an earth-fixed reference frame S_E with axes X_E, and Y_E spanning the horizontal ground and pointing to the north and east respectively, and Z_E pointing downwards. The two front tethers, attached to the leading edge of the kite at points $A_\pm$, are of lengths L_l and connect at point F_v. The two control tethers of lengths L_t connect points $B_\pm$ of the trailing edge with the tips of a control bar of length L_{cb}. For clarity, such a length is not shown in the inset of Fig. 1. The control bar slides over a short tether of length L_s that links the moving point F_v with the origin O_E fixed to the ground.

6

Following Ref. [14], we also introduce the plane Π defined by points F_v and $A_\pm$. Since the tethers connected to the leading edge transfer most of the aerodynamic load, we will assume that they are well-tensioned and thus straight, within the plane Π. A kite-fixed reference frame S_K linked to the kite with origin at its center of mass O_K will be also used. Axes X_K and Z_K are in the plane of symmetry of the kite, X_K is parallel to the center chord, i.e. the imaginary line linking the leading and trailing edge points of the plane of symmetry of the kite, and Y_K completes a right-handed coordinate frame. The S_K-component of the tensor of inertia of the kite about its center of mass then reads,

$$\bar{\boldsymbol{I}}_{O_K} = \begin{pmatrix} I_x & 0 & I_{xz} \\ 0 & I_y & 0 \\ I_{xz} & 0 & I_z \end{pmatrix} \tag{1}$$

Our kite state vector

$$\boldsymbol{x}_k = [\boldsymbol{r} \ \boldsymbol{v} \ \ \boldsymbol{\Upsilon} \ \ \boldsymbol{\omega}] \tag{2}$$

includes the S_E-components of the position vector of the kite, the S_K-components of the absolute velocity and angular velocity of the kite, and its roll, pitch, and yaw angles

$$\boldsymbol{r} = \overline{O_E O_K} = x_E \boldsymbol{i}_E + y_E \boldsymbol{j}_E + z_E \boldsymbol{k}_E \tag{3}$$

$$\boldsymbol{v} = d\boldsymbol{r}/dt = u\boldsymbol{i}_K + v\boldsymbol{j}_K + w\boldsymbol{k}_K \tag{4}$$

$$\boldsymbol{\omega} = p\boldsymbol{i}_K + q\boldsymbol{j}_K + r\boldsymbol{k}_K \tag{5}$$

$$\boldsymbol{\Upsilon} = [\phi \ \ \theta \ \ \psi] \tag{6}$$

A detail of the configuration of the control bar is given in the inset of Fig. 1. The middle point of the bar, named C_0, slides over a tether of length L_s that links points F_v and O_E. If considered massless, such a tether will be in plane Π plane because its tension vector is in equilibrium with the tension vectors of the two tethers connecting to the leading edge which define the plane Π. The movement of the bar is limited by the depower and power stoppers that are placed at distances L_{ds} and L_{ps} from F_v and O_E, respectively. Its distance to the power stopper is denoted as D_{cb}. Assuming that the pilot maneuvers the kite while keeping the control bar inside plane Π, the state

7
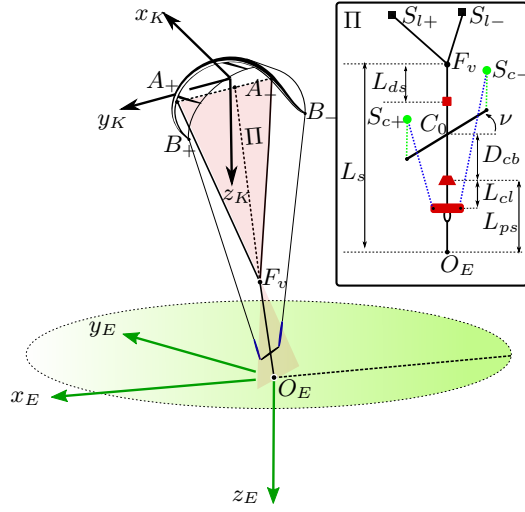
Fig. 1: Scheme of the experimental setup.

of the bar is given by a control vector with only two variables

$$\boldsymbol{x}_c = [u_p \quad \nu], \tag{7}$$

i.e. a power ratio u_p, and the bar deflection angle ν between the bar and the tether of length L_s. The former is defined as [25]

$$u_p = 1 - \frac{D_{cb}}{L_s - L_{ps} - L_{ds}} \tag{8}$$

and it takes values equal to zero and one when the kite is fully depowered (bar at the depower stopper) and powered (bar at the power stopper), respectively. The inset also shows the four load sensors (marked by black squares and green circles) and the distance sensors attached to the control bar safety fuse. These elements are described in Sec. II B, which focusses on the hardware selection and the reconstruction of the state and control vectors from the measurements.

B. Hardware selection

AWE systems typically use large kites, flying hundreds of meters high in the sky. Those systems are being developed on the basis of flexible ramair kites (KiteEnergy, Kite Power Solutions and SkySails), semi-rigid inflatable kites (KitePower), and tethered fixed-wing drones (Makani M600 or Ampyx Power solutions) [2]. Since the rigid body hypothesis is implicitly assumed in our work, our solution to the FPR problem is more suitable for semi-rigid and tethered fixed-wing drones. This

8

assumption, in addition to cost and resource constraints, led to the decision to focus the analysis on two different four-lines, off-the-shelf inflatable surf-kites with tether lengths in the order of several tens of meters. Such a small-scale, but still representative, system is useful because the techniques, tools, and hardware components developed in this work can be easily implemented with much larger kites. Table 1 shows the most important characteristics of the kites. They both have the same mass but there is a 30% difference in surface area. Compared to the larger kite, the smaller one is more rigid because it has two additional struts. The lengths of the leading edge supporting lines, here named the kite bridle, are different but the control bar, tether lengths, and experimental setup used for both kites are identical.

	Cabrinha Switchblade	Cabrinha Contra
Mass	$3.4\,\mathrm{kg}$	$3.4\,\mathrm{kg}$
I_x	$8.68\,\mathrm{kg\,m^2}$	$12.33\,\mathrm{kg\,m^2}$
I_y	$2.43\,\mathrm{kg\,m^2}$	$3.18\,\mathrm{kg\,m^2}$
I_z	$8.40\,\mathrm{kg\,m^2}$	$11.41\,\mathrm{kg\,m^2}$
I_{xz}	$0.33\,\mathrm{kg\,m^2}$	$0.43\,\mathrm{kg\,m^2}$
Surface	$10\,\mathrm{m^2}$	$13\,\mathrm{m^2}$
Span	$4.3\,\mathrm{m}$	$5\,\mathrm{m}$
Struts	5	3
X_A	$0.42\,\mathrm{m}$	$0.53\,\mathrm{m}$
Y_A	$1.05\,\mathrm{m}$	$1.40\,\mathrm{m}$
Z_A	$-0.20\,\mathrm{m}$	$-0.31\,\mathrm{m}$
X_B	$-0.97\,\mathrm{m}$	$-0.98\,\mathrm{m}$
Y_B	$2.15\,\mathrm{m}$	$2.50\,\mathrm{m}$
Z_B	$1.38\,\mathrm{m}$	$1.60\,\mathrm{m}$
L_l	$23.85\,\mathrm{m}$	$24.37\,\mathrm{m}$
L_t	$23.19\,\mathrm{m}$	$23.45\,\mathrm{m}$

Table 1: Kite parameters

Both kites have a supported inflated leading edge and swept back wing. The bridled leading edge

9

allows for flatter wings with higher aspect ratios than those with unsupported ones, thus increasing the aerodynamic efficiency and projected lifting area. Moreover, the concave trailing edge and swept back angle in the wing, allow for greater lift control by increasing the pitch variations induced by the control bar. Such a higher maneuverability still keeps acceptable control forces on the bar, due to the shifting of the attaching points of the control lines further back of the pressure center of the wing. These characteristics, in comparison with the so called C type unsupported leading edge kites, provide a broader flight envelope and allow a larger dynamical range for the measured variables. Such a property is of great interest for future studies in terms of parameter identification and system observability. Panel (a) in Fig. 2 shows the $13\,\mathrm{m}^2$ kite during one of the flight tests.


(a)

(b)

(c)
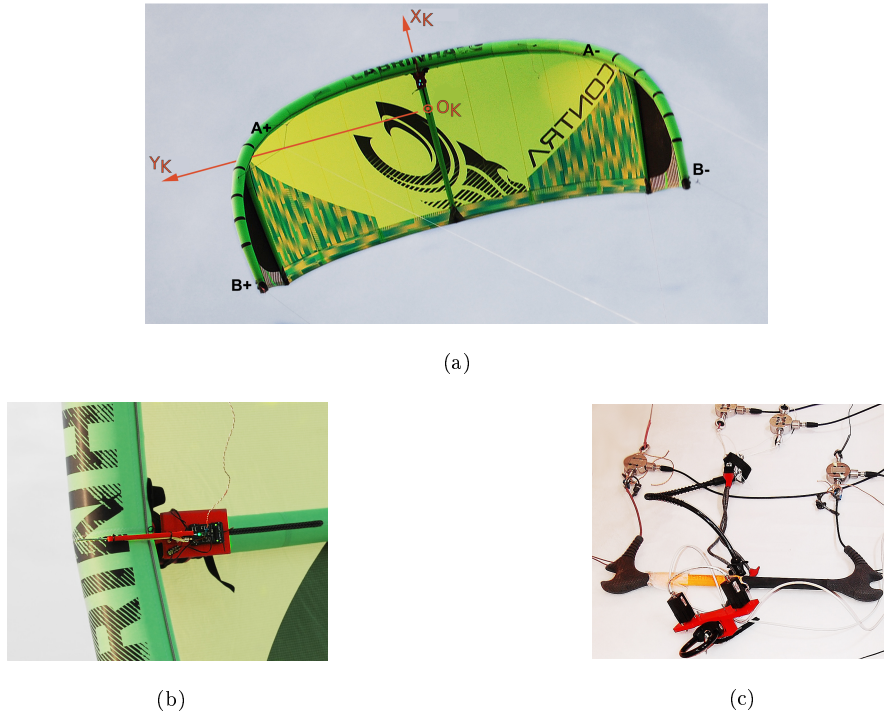
Fig. 2: Panels (a), (b) and (c) show the Cabrinha Contra $13\,\mathrm{m}^2$ kite during a flight test, a detail of the pitot tube and the inertial navigation instruments, and the control bar with the load and distance sensors.

The flight test instrumentation implemented in the experimental setup are split into two groups. The first group includes the onboard instruments. A PixHawk™ running Px4™ open source flight control software, was used for datalogging GPS position $\tilde{r}$ and velocity $\tilde{v}$, magnetic field vector $\tilde{B}$,

static and differential pressures $\tilde{p}_0$ and $\tilde{p}_d$, specific forces $\tilde{\boldsymbol{f}}_{IMU}$, and angular rates $\tilde{\boldsymbol{\omega}}$. Additionally, Px4™ attitude estimation was recorded during the flight for validation purposes of our own estimator (see Figure 3 in Sec. IV,). Onboard instruments were powered by a 4.8V NiMh battery, while its positioning and orientation with respect to the kite frame S_B was guaranteed by a specifically designed 3D printed rig [see Fig. 2b]. Such interface allows to safely attach the sensors to the central strut of the kite, just behind the leading edge. The plastic rig was designed to align the PixHawk™ hardware to the axes of S_K. Therefore, the measured vector components are provided in the S_K-frame.

The second instrumentation group comprises the on-ground sensor equipment. As shown in the schematic of Fig. 1 and Fig. 2c, four load sensors were installed to measure the tether tensions at points $S_{c\pm}$ and $S_{l\pm}$. The sensors at $S_{c\pm}$ are at distance s_0 from the tips of the control bar. In order to measure the state of the control vector, defined by the power ratio and the bar deflection, a specifically designed and manufactured interface with two Posiwires WS31C 750 mm distance sensors was secured to the safety fuse of the kite control bar. These sensors measure the distances $\tilde{d}_\pm$ between the tips of the interface, placed at distance w_{cl} from the tether of length L_s, and points $S_{c\pm}$.

Since $|\overline{C_0 O_K}| >> |\overline{A_\pm B_\pm}|$, one may assume that the rear control lines practically belong to Π and they are parallel to the tether of length L_s. Under such assumptions, the following trigonometric relations hold

$$\tilde{d}_\pm^2 \approx \left(L_{cl} + D_{cb} \mp \frac{L_c}{2} \sin \nu + s_0 \right)^2 \tag{9}$$

$$+ \left(\frac{L_c}{2} \cos \nu - w_{cl} \right)^2 \tag{10}$$

These constraints and Eq. (8) give the power ratio u_p (or the control bar distance D_{cb}) and the bar deflection ν as a function of the measured distances $\tilde{d}_+$ and $\tilde{d}_-$.

Table 2 provides the numerical values of the characteristic lengths related to the experimental setup of the control bar. The load cells and the distance sensors feed a National Instruments 6002 data acquisition system with eight 16 bits, 50 kSamples/s analog inputs and two 16bits analog outputs. The data acquisition system was connected to a laptop running NI Signal Express Software

through a USB interface.

Symbol	Value	Symbol	Value
L_c	0.56 m	L_s	2.07m
L_{ds}	0.52m	L_{ps}	1.1 m
L_{cl}	0.1m	w_{cl}	0.07m
s_0	0.35m		

Table 2: Characteristic lengths related with the control bar

The selection of the load cells was based on the expected traction forces. A conservative calculation, based on a maximum aerodynamic lift coefficient $C_L = 1.2$ and airspeed about $V_a = 7$ m/s, gives a lift force around 460 N for the larger kite. Since most of the load is supported by the front lines, we took two 50 kg, self-amplified, ± 10 V analog output, TS-AMP load cells for the front tethers. For the rear tethers, we selected two 10 kg TS-AMP. Forces during flight tests where limited to 1000 N (roughly twice the expected stationary lift force) by manual control of the kite and real time supervision of the generated forces. The amplified load cells and the distance sensors were powered by a 22.2 V LiPo rechargeable battery pack, while the NI 6002 was powered through the host computer USB port.

As two different group of sensors (onboard and on-ground) with two different data logging systems were used, a synchronization method was needed. For this purpose, a square time signal was generated by the analog output of the National Instruments 6002. This signal was fed from the NI 6002 output in the ground to the 6.6 V PixHawk™ ADC input in the kite, and recorded synchronously.

In case of loss of control, the surfkites are equipped with a manual safety fuse that allows the rear lines to become completely slack, so the kite flags on the front lines with zero angle of attack and falls to the ground. In order to make this safety method compatible with the experimental setup, a fifth line linking the leading edge with the ground was added. Such a line does not play any role from a dynamic point of view because it does not support any load during a normal flight.

III. Space State Flight Path Reconstruction

This section presents a solution to the FPR problem of the experimental setup in Sec. IIB. Its main inputs are the digital records of the sensors during the flight, which contain statistical noise and other inaccuracies, and its outputs are the time histories of the system state variables. In addition to the kite kinematic variables, it also provides an estimation of the kite aerodynamic force and moment, wind speed and direction, and tether loads. This feature distinguishes it from other estimation solutions for kites and it is of great interest for future works on the aerodynamic characterization of kites based on EBM techniques. The core of the algorithm follows previous works on FPR for aircrafts by using continuous-discrete extended Kalman filters (EKFs), where forces and moments were also part of the state vector and modeled as Gauss-Markov stochastic processes [21, 29, 30]. They have been adapted to consider the special characteristics of kites and also our experimental setup. These extensions cover the information added by the constraints introduced by the tethers, the GPS, magnetic field, and tether length measurements, and also a variation of the process model of the sensors to include stochastic error models for each sensor.

The process model of the filter is written in the compact form

$$\frac{d\boldsymbol{x}(t)}{dt} = \boldsymbol{f}_{proc}\left[\boldsymbol{x}(t)\right] + \bar{\boldsymbol{G}}\boldsymbol{w}(t) \tag{11}$$

with $\boldsymbol{x}$ representing the state vector and $\boldsymbol{w}$ the process noise, which is modeled from a multi-variable normal distribution function with zero mean and covariance $\bar{\boldsymbol{Q}}$. Explicit equations for the flow $\boldsymbol{f}_{proc}$ and the constant matrix $\bar{\boldsymbol{G}}$ are given in Appendix A. The state vector of the filter

$$\boldsymbol{x} = [\boldsymbol{x}_k \;\; \boldsymbol{x}_{bias} \;\; \boldsymbol{\chi}_1 \;\; \boldsymbol{\chi}_2 \;\; \boldsymbol{\chi}_3] \tag{12}$$

appearing in Eq. (11) includes: (i) the *kite state vector* ($\boldsymbol{x}_k$ in Eq. (2)), (ii) a *bias state vector* $\boldsymbol{x}_{bias} = [\boldsymbol{\Theta}_B \;\; \boldsymbol{\Theta}_f \;\; \boldsymbol{\Theta}_\omega \;\; \Theta_{aer}]$ with the biases for the measured magnetic field, IMU specific forces, angular velocities, and airspeed, and (iii) a set of three *pseudo states vectors* $\boldsymbol{\chi}_i = [\boldsymbol{F}_{ai} \;\; \boldsymbol{M}_{ai} \;\; T_{A^+i} \;\; T_{A^-i} \;\; T_{B^+i} \;\; T_{B^-i} \;\; V_{wi} \;\; \psi_{wi}]$ with $i = 1, 2, 3$, stochastically described using third-order Markov Models. The first vector $\boldsymbol{\chi}_1$ contains the S_B-components of the aerodynamic force $\boldsymbol{F}_{a1}$ and moments about the center of mass of the kite $\boldsymbol{M}_{a1}$, the magnitudes of the tether tensions at the four attachment points $T_{A\pm1}$ and $T_{B\pm1}$, the magnitude of the wind velocity $V_{w,1}$ and its heading

angle $\psi_{w,1}$. The process equations of this vector and the ones for $\boldsymbol{\chi}_2$ and $\boldsymbol{\chi}_3$ yield a three-term quadratic interpolation as a function of time, whose coefficients are updated by the filter at each sampling instant. The dimensions of the kite state $\boldsymbol{x}_k$, bias state $\boldsymbol{x}_{bias}$, and each Markov vector $\boldsymbol{\chi}_i$ are equal to 12, 10, and 12, respectively. Therefore, the dimension of the total state vector of the filter $\boldsymbol{x}$ is $N_F = 58$.

Although the state vector of the filter just contains the magnitude of the tether forces, we can estimate the vectors if we assume that the tensions are along the line determined by the attachment points ($A^\pm$ or $B^\pm$) and O_E. Hereafter, we will take

$$\boldsymbol{T}_{A^\pm} = -T_{A^\pm 1}\overline{O_E A^\pm}/\mid \overline{O_E A^\pm}\mid \tag{13}$$

$$\boldsymbol{T}_{B^\pm} = -T_{B^\pm 1}\overline{O_E B^\pm}/\mid \overline{O_E B^\pm}\mid \tag{14}$$

with

$$\overline{O_E A^\pm} = \boldsymbol{r} + \overline{O_B A^\pm}, \tag{15}$$

$$\overline{O_E B^\pm} = \boldsymbol{r} + \overline{O_B B^\pm}, \tag{16}$$

$$\overline{O_B A^\pm} = X_A \boldsymbol{i}_K \pm Y_A \boldsymbol{j}_K + Z_A \boldsymbol{k}_K \tag{17}$$

$$\overline{O_B B^\pm} = X_B \boldsymbol{i}_K \pm Y_B \boldsymbol{j}_K + Z_B \boldsymbol{k}_K \tag{18}$$

The coordinates of the attachment points of the two kites are given in Table 1. Equations (13)-(14) assume that the tethers are straight, and also used the fact that the tethers are much longer than the distance between the center of mass of the kite and the IMU, and also any distance related with the setup of the control bar (see Table 2). This pair of equation gives the tether tensions as a function of the state vector of the filter.

After denoting with symbol $\sim$ the variables measured by the sensors, the measurement model of the filter is

$$\tilde{\boldsymbol{y}} = \boldsymbol{h}(\boldsymbol{x}) + \boldsymbol{\eta} \tag{19}$$

with $\tilde{\boldsymbol{y}}$ representing the observation vector, $\boldsymbol{h}(\boldsymbol{x})$ the observation model that maps the true state space into the observed space (see the explicit model of $\boldsymbol{h}$ in Appendix A), and $\boldsymbol{\eta}$ the observation

noise which is assumed to be zero mean Gaussian white noise with covariance $\bar{\boldsymbol{R}}$. The observation vector of the experimental setup

$$\tilde{\boldsymbol{y}} = \begin{bmatrix} \tilde{\boldsymbol{r}} & \tilde{\boldsymbol{v}} & \tilde{\boldsymbol{f}}_{IMU} & \tilde{\boldsymbol{\omega}} & \tilde{\boldsymbol{B}} & \tilde{v}_{aer} & \tilde{D} & \tilde{T}_{A^-} & \tilde{T}_{B^+} & \tilde{T}_{B^+} & \tilde{T}_{A^+} \end{bmatrix} \tag{20}$$

includes the S_E-components of the position and velocity vectors of the kite ($\tilde{\boldsymbol{r}}$ and $\tilde{\boldsymbol{v}}$), the S_K-components of the specific force measured by the IMU, angular velocity, and magnetic field ($\tilde{\boldsymbol{f}}_{IMU}$, $\tilde{\boldsymbol{\omega}}$, and $\tilde{\boldsymbol{B}}$), the magnitude of the airspeed ($\tilde{v}_{aer}$), the distance between the fixed point O_E and the center of mass of the kite ($\tilde{D}$), and the four magnitudes of the tether forces $\tilde{T}_{A\pm}$ and $\tilde{T}_{B\pm}$. We remark that the specific force measured by the IMU is equal to the kite acceleration minus the gravitational acceleration.

The application of the EKF to Eqs. (11)-(19) is standard (see for instance Ref. [31]). As usual, we will denote with superscripts $-$ and $+$ the *a priori* (before measurement) and *a posteriori* (after measurement) estimated values, respectively. Given the estimated value of the state vector $\hat{x}_j^+$ and the covariance matrix $\bar{\boldsymbol{P}}_j^+$ at instant t_j, the EKF computes their values at a later instant t_{j+1} as follows. First, in the prediction phase, the reference trajectory $\boldsymbol{x}_R(t)$ is computed by integrating Eq. (11) without noise

$$\frac{d\boldsymbol{x}_R(t)}{dt} = f\left[\boldsymbol{x}_R(t)\right] \tag{21}$$

from $t = t_j$ to $t = t_{j+1}$ and with the initial condition $\boldsymbol{x}_R(t_j) = \hat{\boldsymbol{x}}_j^+$. An approximation of the state transition matrix $\bar{\bar{\boldsymbol{\Phi}}}$ is obtained by integrating the linearized version of Eq. (21)

$$\frac{d\bar{\bar{\boldsymbol{\Phi}}}}{dt} = \bar{\boldsymbol{J}}\bar{\bar{\boldsymbol{\Phi}}} \tag{22}$$

with initial condition $\bar{\bar{\boldsymbol{\Phi}}}(t = 0) = \bar{\boldsymbol{I}}$, and $\bar{\boldsymbol{J}}$ the Jacobian of $\boldsymbol{f}$ evaluated at $\hat{\boldsymbol{x}}_j^+$. The *a priori* state vector and covariance matrix at t_{j+1} are

$$\boldsymbol{x}_{j+1}^- = \boldsymbol{x}_R(t_{j+1}), \tag{23}$$

$$\bar{\boldsymbol{P}}_{j+1}^- = \bar{\bar{\boldsymbol{\Phi}}}\bar{\boldsymbol{P}}_j^+\bar{\bar{\boldsymbol{\Phi}}}^T + \bar{\boldsymbol{G}}\bar{\boldsymbol{Q}}\bar{\boldsymbol{G}}^T. \tag{24}$$

The Kalman gain is

$$\bar{\boldsymbol{K}}_{j+1} = \bar{\boldsymbol{P}}_{j+1}^-\bar{\boldsymbol{H}}_{j+1}^T \left(\bar{\boldsymbol{H}}_{j+1}\bar{\boldsymbol{P}}_{j+1}^-\bar{\boldsymbol{H}}_{j+1}^T + \bar{\boldsymbol{R}}\right)^{-1}, \tag{25}$$

15

with $\bar{\boldsymbol{H}}_{j+1}$ the Jacobian of $\boldsymbol{h}$ evaluated at $\hat{x}_{j+1}^-$. The *a posteriori*, i.e. corrected by the measurements, estimations at t_{j+1} are

$$\hat{\boldsymbol{x}}_{j+1}^+ = \hat{\boldsymbol{x}}_{j+1}^- + \bar{\boldsymbol{K}}_{j+1}\left[\tilde{\boldsymbol{y}}_{j+1} - \boldsymbol{h}\left(\hat{\boldsymbol{x}}_{j+1}^-\right)\right], \tag{26}$$

$$\bar{\boldsymbol{P}}_{j+1}^+ = \left(\bar{\boldsymbol{I}} - \bar{\boldsymbol{K}}_{j+1}\bar{\boldsymbol{H}}_{j+1}\right)\bar{\boldsymbol{P}}_{j+1}^-. \tag{27}$$

In addition to the Kalman innovation error $\tilde{\boldsymbol{y}}_{j+1} - \boldsymbol{h}\left(\hat{\boldsymbol{x}}_{j+1}^-\right)$ in Eq. (26), the filter also gives the difference $\boldsymbol{h}\left(\hat{\boldsymbol{x}}_{j+1}^+\right) - \boldsymbol{h}\left(\hat{\boldsymbol{x}}_{j+1}^-\right)$ that can be used for checking purposes.

The application of the filter to our flight data exhibited a high robustness with little sensitivity to its initialization. In any case, we normally initialized $\boldsymbol{x}_k$ by using the information provided by the GPS and assuming symmetric flight with zero angular velocity. Vectors $\boldsymbol{x}_{bias}$, $\boldsymbol{\chi}_2$, and $\boldsymbol{\chi}_3$ were initialized to zero. For $\boldsymbol{\chi}_1$, we set the specific forces equal to minus the weight, zero moments, and wind velocity and its heading angle taken from average measurements before the flight. Following [21], the covariance matrix was initialized with the measured noise of the measured variables, and to one-forth of the estimated initial value of the state for the unmeasured ones. The filter parameters has been tuned by using the sensors data sheets and also by analyzing the effect of the different parameters on the filter output. A full description of the filter and the parameters used in this work are given in Appendix A and Table 3, respectively.

IV. Experimental results

Flight tests have been carried out with the $13\,\mathrm{m}^2$ and $10\,\mathrm{m}^2$ kites under similar wind conditions. The testing procedure started by powering all the sensors while the kites were on the ground. Px4™ software was modified to record data from all sensors after powering up. Once a valid GPS signal was acquired, the kite was launched from one edge of the wind window and steered towards a stable equilibrium state close to the zenith. At that moment, the data acquisition software and the synchronization time signal were started, thus allowing a synchronous data acquisition of the onboard and on-ground instruments. Several manoeuvres (see below) were performed repeatedly, and the kite was landed at one edge of the wind window afterwards. The data recorded by all the instruments, which were re-sampled using a common $50\,\mathrm{Hz}$ time vector started at the first rising edge of the synchronization signal, were analyzed off line.

16

Figures 3(a)-(c) show the evolution of the pitch, roll, and yaw angles for the $13\,\mathrm{m}^2$-kite during the first two minutes of flight. The dashed black lines, and the solid red lines correspond to the Px4™ and the FPR estimated attitude, respectively. Both estimations, obtained from totally independent algorithms and software, are in good agreement. They prove that the experimental setup and the filter are correctly implemented. A second verification of the integrity of the filter is given in Fig. 4, which shows the GPS measured (dashed black lines) and FPR estimated (solid red lines) values of the kite position components X_E and Y_E, its altitude $H = -Z_E$, and the constraint distance D appearing in Eq. A9. The addition of such a constraint in our EKF greatly improved the GPS accuracy. As shown in Fig. 4(d), raw GPS distance to the attachment point O_E, oscillate with typical GPS accuracy values, while the FPR solution follows the imposed constrain.
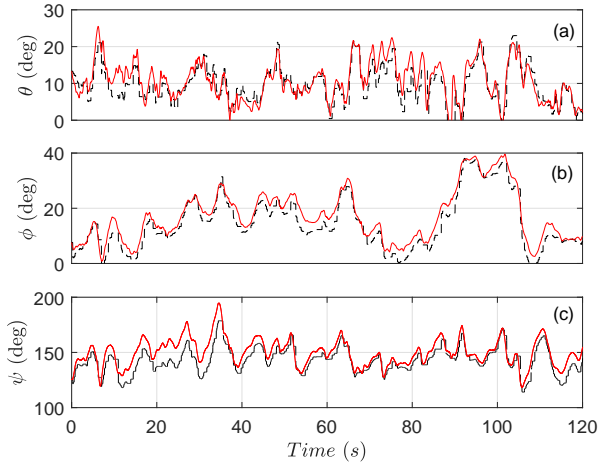

Fig. 3: Euler angles of the $13\,\mathrm{m}^2$-kite estimated by the PixHawk™ software (dashed black) and the FPR algorithm (solid red).

The next two sections show experimental results of two different maneuvers: (i) a pull-up, i.e. continuous enhancement of the power ratio with vanishing (or small) lateral deflection of the control bar, and (ii) a steering maneuver with periodic variations of the deflection angle of the control bar. The goal of the analysis is twofold. First, it provides quantitative information about the performances of the experimental setup and the filter, and shows coherence between control inputs and kite response. Second, it highlights some of the distinguished features of the filter such as the estimation of the aerodynamic force and moment.
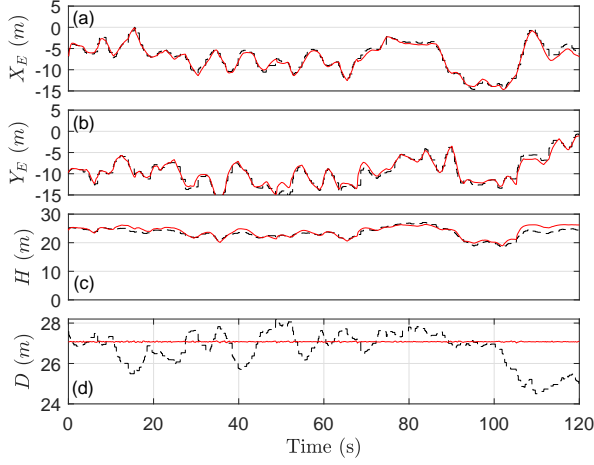
Fig. 4: Positions X_E, Y_E and H, and distance D measured by the sensors (dashed black) and estimated with the FPR algorithm (solid red).

A. Pull-up maneuver

Figure 5 shows the evolution of the power ratio and deflection angle of the control bar during a pull-up maneuver of the $10 \, \text{m}^2$-kite. As shown by the results below, the maneuver is not perfectly symmetric but close to it. The power ratio was increased smoothly from 40% to 90% approximately, and the deflection angle was held almost constant at $-4°$, i.e. the pilot was pulling slightly the right control line (the one linked to point B_- in Fig. 1). The position of the center of mass of the kite (not shown) remained almost constant during the time span displayed in Fig. 5.
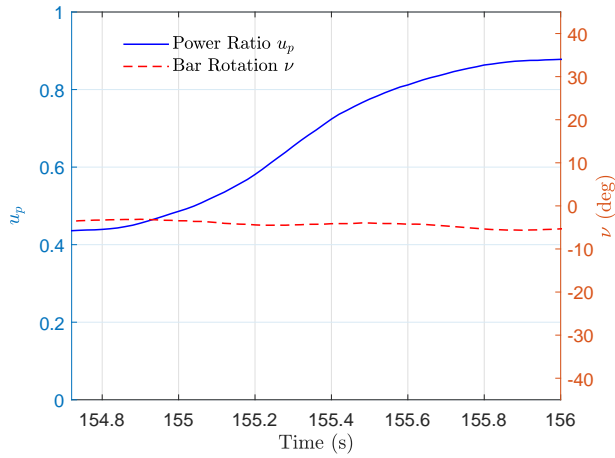

Fig. 5: Power Ratio and bar deflection angle versus time during a symmetric pull-up manoeuver.

18

The FPR of the Euler angles (pitch, yaw and roll) versus the power ratio during the pull-up maneuver are shown in Fig. 6(a), where, for clarity, the yaw angle has been divided by a factor of 10. As expected, the yaw and roll angles are almost constant during the pull-up, and the pitch angle increased notably ($\Delta\theta \sim 7.1°$). These results are in agreement with the sign of the estimated angular velocities [see Fig. 6(b)]. The linear dependence between the pitch angle and the power ratio can be understood from simple kinematic considerations. After assuming straight and inextensible tethers, pure rotation along $\boldsymbol{j}_K$, and small pitch angle variations, we can write $\Delta\theta \approx -\Delta D_{cb}/R_G$, with $\Delta\theta$ being the increment of the pitch angle, ΔD_{cb} the distance increment between the control bar and the power stopper, and $R_G = \sqrt{(X_A - X_B)^2 + (Z_A - Z_B)^2} = 2.12$ m the distance between the two lines passing through points A_+ and A_- and B_+ and B_- for the 10 m^2 kite. Calling $u_{p0} \approx 0.42$ and $u_{p\infty} = 0.9$ the initial and final power ratios, one has $\Delta D_{cb} = (L_s - L_{ps} - L_{ds})(u_{p0} - u_{p\infty}) \approx -0.216$ m, that gives a pitch increment of 5.84°.

A quasi-stationary ($\Delta t \approx 1.2$ s) variation of pitch angle translates into an instantaneous increase of the kite angle of attack and modifies the aerodynamic forces. Its lateral S_K-component remains almost invariant, as shown by the dashed blue line in Fig. 7(a). However, as expected, the longitudinal components F_{ax1} and F_{az1} increased considerably during the maneuver. Figure 7(b) shows the components of the estimated aerodynamic moment. The pitch moment M_{ay1} remains relatively constant indicating a position of the center of mass close to the aerodynamic center $c/4$. This can be checked using data provided in Table 1, where $c/4 \approx (X_A - X_B)/4 = 0.38$ m, and the distance of the CG to the leading edge of the kite is approximately $X_A = 0.42$m. On the other hand, an average wind heading angle $\psi_w \approx -60°$ and a yaw angle during the maneuver of $\psi \approx 150°$ results in a negative side slip angle of the kite. As expected, the estimated roll moment M_{ax1} is negative due to the negative dihedral of the wing. Finally, Fig. 7(c) shows the magnitude of the resultant of the four tether tensions estimated in the FPR $\hat{\boldsymbol{T}}$, and for reference, the tensions measured by the load sensors $\tilde{\boldsymbol{T}}$. Again, the tension exhibits a linear dependence with the power ratio and is almost doubled during the pull-up.
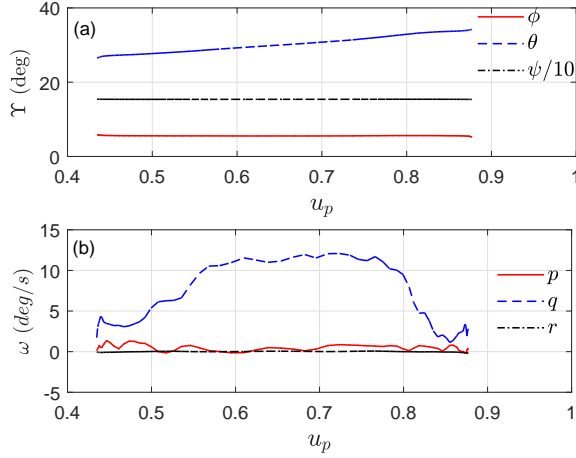
Fig. 6: Pull-up manoeuver: Euler angles and angular velocity versus power ratio during. Yaw angle is divided by a factor 10.
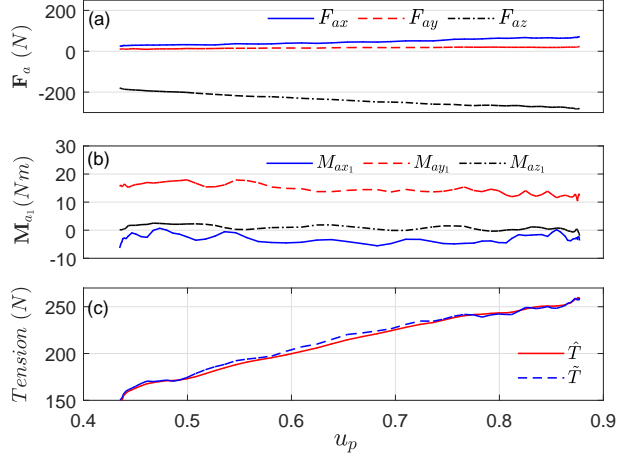

Fig. 7: Pull-up manoeuver: panels (a-b) show the S_K-components of the aerodynamic force and moment versus power ratio, and panel (c) the magnitude of the estimated (solid and red) and measured (dashed and blue) total tension.

B. Steering manoeuver

The lateral-directional dynamics of the $10\,\mathrm{m}^2$-kite was investigated by varying periodically the deflection angle of the control bar. As shown in Fig. 8, the maximum and minimum deflections were about $20°$ and $-30°$. Since the force at the bar increased notably during the induced crosswind motion of the kite, the pilot could not keep the power ratio constant and it also varied periodically

around the nominal value $u_p \approx 0.4$. The kite flew in crosswind conditions and moved from side to side in the wind window. A top view of the measured trajectory is displayed in Fig. 9, where we also plotted the wind direction and the Earth axes at the initial instant of the steering maneuver.
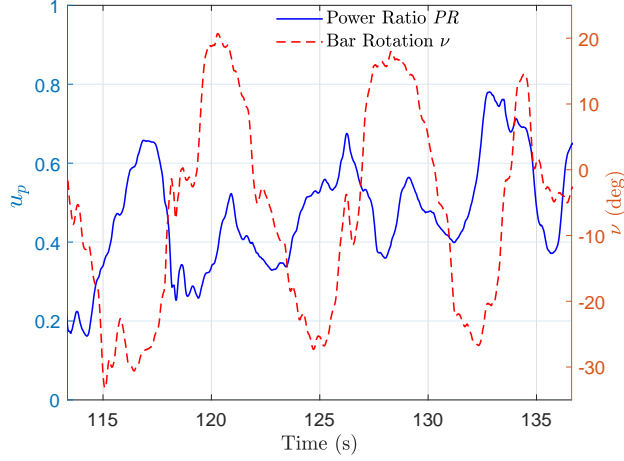
Fig. 8: Power Ratio and bar deflection angle versus time during a steering manoeuver.
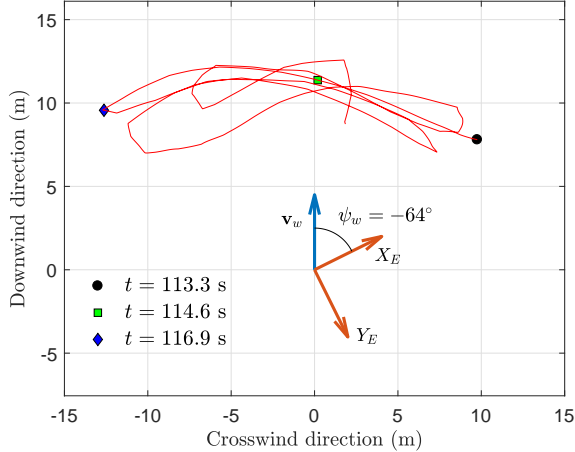
Fig. 9: Top view of the kite trajectory during the steering maneuver.

We now describe the lateral-directional steering maneuver as seen from the point of view of the pilot placed at the origin the wind reference frame displayed in Fig. 9. The steering maneuver starts with the kite placed at the right side of the wind window (black circle in Fig. 9). Since the kite had initially a lateral velocity pointing to the left and the pilot imposed almost zero deflection to the control bar at that instant, the kites moved laterally. While the kite was moving to the left

21

with a positive and increasing roll angle [Fig. 10(a)], the pilot pulled the right tip of the control bar, thus decreasing angle ν (see Fig. 8). Such a control input stopped the lateral motion of the kite, and avoided a kite crash at the left hand side of the wind window. The kite reached the center of the wind window and the maximum lateral displacement at instants $t = 114.6$ s and $t = 116.9$ s, respectively. The latter coincided approximately with the minimum of ν. After reaching the maximum lateral displacement at the left side, the kite moved to the right and the pilot increased the value of ν from $-27°$ at $t \approx 117$ s to $+20.46°$ at 120.4 s. The kite performed a second crosswind motion during that time interval. It is also interesting to look at the behavior of the roll angular velocity component p. At the beginning of the maneuver, p was positive and at a maximum. The action of the pilot, decreased the value of p and, once it vanished, the kite banked to the right and moved to the opposite side of the wind window.

An analysis of the control inputs in Fig. 8 and the Euler angles in Fig. 10 reveals a strong correlation between the deflection of the bar and the yaw angle of the kite. The roll response does also follow these two variables but with certain delay. The forces and torques provided by the EKF [Fig. 11(a)-(b)] are coherent with the dynamics described previously. The lateral force component F_{ay1} and the roll torque M_{ax1} oscillates among positive and negative values. The longitudinal force components, especially F_{az1}, are larger than the one observed during the pull-up due to the crosswind conditions of the steering maneuver. This effect is a also evident in Fig. 11(c), where the magnitude of the resultant of the four tether tensions is plotted.

V. Conclusions

This work presents a flight path reconstruction (FPR) method for tethered kites based on an extended Kalman filter (EKF), and an experimental setup designed to provide the required measured flight data for the algorithm. These are kite position, velocity, angular velocity, airspeed, magnetic field and tether tensions. Those data are respectively provided by a GPS, IMU, static and impact pressure transducers, magnetometer, and load cells installed at the kite tethers, while two distance sensors gave the state of the control bar (power ratio and angle deflection of the control bar). The solution of the FPR problem (also known as compatibility check) is a first step towards kite and
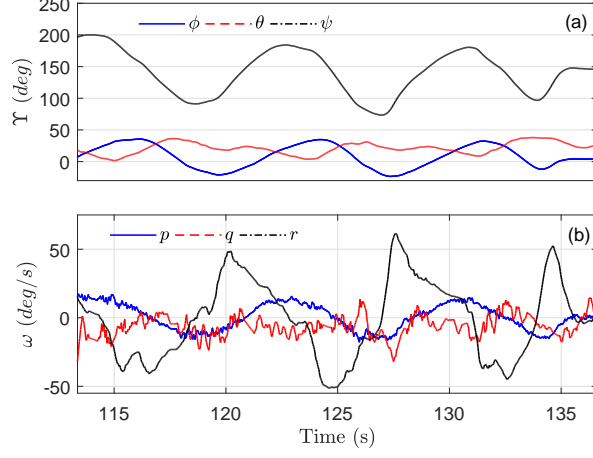
Fig. 10: Panels (a) and (b) show the Euler angles and the angular velocity during the steering maneuver.
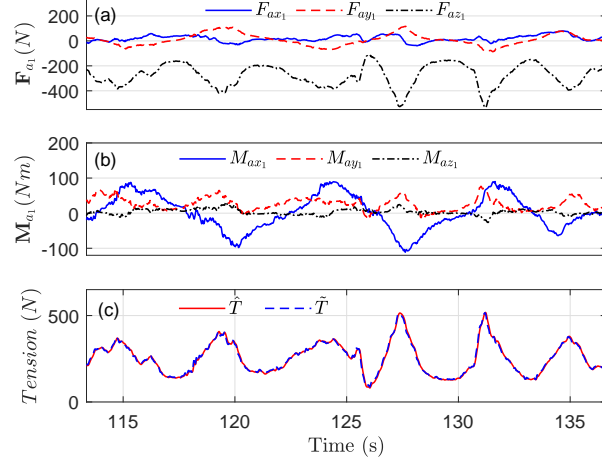
Fig. 11: Panels (a) to (c) show the evolution of the aerodynamic force, torque, and the modulus of the resultant of the four tether tensions.

tethered drones aerodynamic parameter identification using flight tests data. This reconstruction means the optimal estimation of the kite/drone space state trajectory, using the kinematic equations of a tethered kite, measured data and stochastic error models for the involved sensors.

In particular, third order Markov-Models describing the aerodynamic force and torque about the center of mass of the kite has been incorporated to the state vector of the system, thus the aerodynamic response of the kite during the flight is optimally reconstructed. This feature distinguishes

23

our EKF from past works on kites and can be used in future studies for the systematic aerodynamic characterization of kites through the so-called estimation-before-modeling technique. Therefore, a potential application of this work is the aerodynamic characterization of kites and tethered drones applied to airborne wind energy generation and kitesurf design. The EKF can be also a fundamental component in close-loop control scenarios.

Two important advantages of the experimental setup are the portability and low-cost. Two kites of different sizes and stiffness were investigated with the experimental setup, which can be adapted to other kites or even to tethered drones by just 3D-printing the corresponding interfaces to host the on-board measurement instruments. However, the analysis of the results suggests that a more precise platform for the aerodynamic characterization of kites could be achieved by implementing the following improvements: (i) adding an air data boom with sensors to measure the flow direction (wind vanes) and also to improve the quality of the velocity magnitude by measuring in an undisturbed region of the flow field, (ii) substituting the control bar and the load sensors at the tethers by a remotely controlled mechanical assembly with integrated load sensors. Recent studies show that both improvements are feasible for kites similar to the one presented in this work [25, 26]. These changes would affect slightly our EKF by extending the observation vector and models for the angle of attack and sideslip angle measured by the wind vanes.

APPENDIX A: ESTIMATOR DESCRIPTION

1. Observation model

This section introduces the error and measurement models of the sensors that are needed to implement Eq. (19) in the EKF. The GPS provides the S_E-components of the position and the

24

velocity vectors ($\tilde{\boldsymbol{r}} = \tilde{x}_E \boldsymbol{i}_E + \tilde{y}_E \boldsymbol{j}_E + \tilde{z}_E \boldsymbol{k}_E$ and $\tilde{\boldsymbol{v}} = \tilde{v}_x \boldsymbol{i}_E + \tilde{v}_y \boldsymbol{j}_E + \tilde{v}_z \boldsymbol{k}_E$). After ignoring latency but including a wide-band and not correlated noise, the GPS model reads

$$
\begin{pmatrix} \tilde{x}_E \\ \tilde{y}_E \\ \tilde{z}_E \end{pmatrix} = \begin{pmatrix} x_E \\ y_E \\ z_E \end{pmatrix} + \boldsymbol{\eta}_r \tag{A1}
$$

$$
\begin{pmatrix} \tilde{v}_x \\ \tilde{v}_y \\ \tilde{v}_z \end{pmatrix} = \bar{\boldsymbol{R}}_{EK} \begin{pmatrix} u \\ v \\ w \end{pmatrix} + \boldsymbol{\eta}_v \tag{A2}
$$

where we introduced the rotation matrix that relates S_E and S_K vector components

$$
\bar{\boldsymbol{R}}_{EK} = \begin{pmatrix} c\psi c\theta & c\psi s\theta s\phi - s\psi c\phi & c\psi s\theta c\phi + s\psi s\phi \\ s\psi c\theta & s\psi s\theta s\phi + c\psi c\phi & s\psi s\theta c\phi - c\psi s\phi \\ -s\theta & c\theta s\phi & c\theta c\phi \end{pmatrix} \tag{A3}
$$

and, for brevity, we wrote $s\alpha$ and $c\alpha$ to denote the sine and cosine of any angle α. We remark that the S_E-components of the position vector in Eq. (A1) (x_E, y_E and z_E) and the S_K-components of the kite velocity in Eq. (A2) (u, v and w) belong to the kite state vector $\boldsymbol{x}_k$. The noises in the right-hand side of Eqs. (A1) and (A2) are taken from normal distribution functions with zero means and variances $\sigma_{\eta_r}^2$ and $\sigma_{\eta_v}^2$, respectively.

After $\tilde{\boldsymbol{r}}$ and $\tilde{\boldsymbol{v}}$, the next two variables in the observation vector $\tilde{\boldsymbol{y}}$ are the specific forces and the angular velocity components in the kite frame. The model for these two vectors, which are measured by our low cost IMU, is a post-calibration error model given by [32]

$$
\tilde{\boldsymbol{f}}_{IMU} = \frac{1}{m_k} \left[\boldsymbol{F}_{a1} + \sum_{i=\pm} (\boldsymbol{T}_{A^i} + \boldsymbol{T}_{B^i}) \right] + \boldsymbol{\Theta}_f + \boldsymbol{\eta}_f, \tag{A4}
$$

$$
\tilde{\boldsymbol{\omega}} = \boldsymbol{\omega} + \boldsymbol{\Theta}_\omega + \boldsymbol{\eta}_\omega \tag{A5}
$$

where $\boldsymbol{\eta}_f \in N(0, \sigma_{\eta_f}^2)$, $\boldsymbol{\eta}_\omega \in N(0, \sigma_{\eta_\omega}^2)$, and the tensions depend on the state vector of the filter according to Eqs. (13) and (14). Similarly, for the magnetometer and the modulus of the airspeed

we write

$$\tilde{\boldsymbol{B}} = \bar{\boldsymbol{R}}_{EK}^T \boldsymbol{B}_0 + \boldsymbol{\Theta}_B + \boldsymbol{\eta_B}, \qquad \boldsymbol{\eta_B} \in N(0, \sigma_{\eta_B}^2) \tag{A6}$$

$$\tilde{v}_{aer} = \mid \bar{\boldsymbol{R}}_{EK}\boldsymbol{v} - v_{w,1} \begin{pmatrix} \cos\psi_{w,1} \\ \sin\psi_{w,1} \\ 0 \end{pmatrix} \mid + \Theta_{aer} + \eta_{v_{aer}},$$

$$\eta_{v_{aer}} \in N(0, \sigma_{\eta_{v_{aer}}}^2) \tag{A7}$$

where $\boldsymbol{B}_0$ is the magnetic field in the test area. We remark that the differential pressure Δp measured by the pitot tube was transformed into True Air Speed (TAS) by using

$$TAS = \sqrt{\frac{2\tilde{\Delta}_p}{\rho}} \tag{A8}$$

with $\rho = 1.15 kg/m^2$ the air density at the test area obtained from the International Standard Atmosphere. The TAS was then used by the observation model as $\tilde{v}_{aer}$.

The last component of the observation vector is the distance from O_E and the center of mass of the kite, and it arises from the constraint introduced by the tethers, whose stiffness is very high. Such a constraint reads

$$\tilde{D} = \mid \boldsymbol{r} \mid + \eta_D, \qquad \eta_D \in N(0, \sigma_{\eta_D}^2) \tag{A9}$$

Unlike previous components of the observation vector, the distance $\tilde{D}$ is constant and equal to $L_s + \sqrt{L_l^2 - y_{A+}^2}$, where we neglected the small distance between the location of the IMU and O_K, and introduced the distance y_{A+} between the attachment point A^+ and the plane of symmetry of the kite.

Since the biases of the measured tether forces are considered to be comparatively small, our observation model for the tether reads

$$\tilde{T}_{A\pm} = T_{A\pm 1} + \eta_{T_{A\pm}} \tag{A10}$$

$$\tilde{T}_{B\pm} = T_{B\pm 1} + \eta_{T_{B\pm}} \tag{A11}$$

with $\eta_{T_{A\pm}}$ and $\eta_{T_{B\pm}} \in N(0, \sigma_{\eta_T}^2)$.

From Eqs. (A1), (A2), (A4), (A5), (A6), (A7), and (A9) one finds the function $\boldsymbol{h}$ in Eq. (19). Vector $\boldsymbol{\eta}$ is

$$
\boldsymbol{\eta} = [\boldsymbol{\eta}_r \ \ \boldsymbol{\eta}_v \ \ \boldsymbol{\eta}_f \ \ \boldsymbol{\eta}_\omega \ \ \boldsymbol{\eta}_B \ \ \boldsymbol{\eta}_{v_aer} \ \ \boldsymbol{\eta}_D
$$

$$
\eta_{T_{A+}} \ \ \eta_{T_{A-}} \ \ \eta_{T_{B+}} \ \ \eta_{T_{B-}}]^T \tag{A12}
$$

and the covariance matrix $\bar{\boldsymbol{R}}$ have zeros everywhere except at the diagonal

$$
diag(\bar{\boldsymbol{R}}) = \Big[\sigma^2_{\eta_r} \ \ \sigma^2_{\eta_r} \ \ \sigma^2_{\eta_r} \ \ \sigma^2_{\eta_v} \ \ \sigma^2_{\eta_v} \ \ \sigma^2_{\eta_v} \ \ \sigma^2_{\eta_f} \ \ \sigma^2_{\eta_f} \ \ \sigma^2_{\eta_f}
$$

$$
\sigma^2_{\eta_\omega} \ \ \sigma^2_{\eta_\omega} \ \ \sigma^2_{\eta_\omega} \ \ \sigma^2_{\eta_B} \ \ \sigma^2_{\eta_B} \ \ \sigma^2_{\eta_B} \ \ \sigma^2_{\eta_{v_{aer}}} \ \ \sigma^2_{\eta_D}
$$

$$
\sigma^2_{\eta_T} \ \ \sigma^2_{\eta_T} \ \ \sigma^2_{\eta_T} \ \ \sigma^2_{\eta_T} \Big] \tag{A13}
$$

2. Process Model

This section describes in detail the form of the flux $\boldsymbol{f}_{proc}$ and the noise appearing in the right hand side of Eq. (11). The dynamics of the kite state vector $\boldsymbol{x}_k$ is governed by

$$
\frac{d}{dt} \begin{pmatrix} x_E \\ y_E \\ z_E \end{pmatrix} = \bar{\boldsymbol{R}}_{EK} \begin{pmatrix} u \\ v \\ w \end{pmatrix}
$$

$$
\frac{d}{dt} \begin{pmatrix} u \\ v \\ w \end{pmatrix} = \begin{pmatrix} f_x \\ f_y \\ f_z \end{pmatrix} + \bar{\boldsymbol{R}}_{EB}^T \begin{pmatrix} 0 \\ 0 \\ g \end{pmatrix} + \begin{pmatrix} rv - qw \\ pw - ru \\ qu - pv \end{pmatrix} \tag{A14}
$$

$$
\frac{d}{dt} \begin{pmatrix} \phi \\ \theta \\ \psi \end{pmatrix} = \begin{bmatrix} p + (q \sin \phi + r \cos \phi) \tan \theta \\ q \cos \phi - r \sin \phi \\ (q \sin \phi + r \cos \phi) \sec \theta \end{bmatrix} \tag{A15}
$$

$$
\frac{d}{dt} \begin{pmatrix} p \\ q \\ r \end{pmatrix} = \bar{\boldsymbol{I}}_{O_K}^{-1} \begin{bmatrix} M_x - I_{xz} qp + rq (I_y - I_z) \\ M_y + I_{xz} (p^2 - r^2) + pr (I_z - I_x) \\ M_z + I_{xz} qr + pq (I_x - I_y) \end{bmatrix} \tag{A16}
$$

where g is the gravitational acceleration, $\bar{\boldsymbol{I}}_{O_K}$ the tensor of inertia of the kite about its center of mass, and I_x, I_y, I_z and I_{xz} the non-zero components in S_K of $\bar{\boldsymbol{I}}_{O_K}$. In the right hand side

of Eqs. (A14) and (A16) we gathered in the specific force $\boldsymbol{f} = f_x \boldsymbol{i}_B + f_y \boldsymbol{j}_B + f_z \boldsymbol{k}_B$ and torque $\boldsymbol{M} = M_x \boldsymbol{i}_B + M_y \boldsymbol{j}_B + M_z \boldsymbol{k}_B$ the actions of the aerodynamic and tether forces. These two vectors depends on the state vector of the filter as follows

$$\boldsymbol{f} = \frac{1}{m_k} \left[\boldsymbol{F}_{a1} + \sum_{i=\pm} (\boldsymbol{T}_{A^i} + \boldsymbol{T}_{B^i}) \right] \tag{A17}$$

$$\boldsymbol{M} = \boldsymbol{M}_{a1} + \sum_{i=\pm} \left(\overline{O_K A^\pm} \times \boldsymbol{T}_{A^i} + \overline{O_K B^\pm} \times \boldsymbol{T}_{B^i} \right) \tag{A18}$$

with $\boldsymbol{T}_{A\pm}$ and $\boldsymbol{T}_{B\pm}$ given by Eqs. (13) and (14), and $\overline{O_K A^\pm}$ and $\overline{O_K B^\pm}$ by Eqs. (17) and (18).

The process models for the sensor biases are

$$\frac{d\boldsymbol{\Theta}_B}{dt} = 0 \tag{A19}$$

$$\frac{d\boldsymbol{\Theta}_f}{dt} = -\frac{\boldsymbol{\Theta}_f}{\tau_a} + \boldsymbol{w}_f \qquad \boldsymbol{w}_f \in N(0, \sigma_{w_f}^2) \tag{A20}$$

$$\frac{d\boldsymbol{\Theta}_\omega}{dt} = -\frac{\boldsymbol{\Theta}_\omega}{\tau_\omega} + \boldsymbol{w}_\omega \qquad \boldsymbol{w}_\omega \in N(0, \sigma_{w_\omega}^2) \tag{A21}$$

$$\frac{d\Theta_{aer}}{dt} = -\frac{\Theta_{aer}}{\tau_{aer}} + w_{aer} \qquad \boldsymbol{w}_{aer} \in N(0, \sigma_{w_{aer}}^2) \tag{A22}$$

Therefore, the correlated noise of the IMU ($\boldsymbol{\Theta}_f$ and $\boldsymbol{\Theta}_\omega$) are defined by first order Gauss-Markov processes where the variances of the driving noise $\boldsymbol{\sigma}_{w_f}^2$ and $\boldsymbol{\sigma}_{w_\omega}^2$ and the time constants τ_a and τ_ω are tuning parameters adjusted to over bound the Allan Variance plot of correlated noise [32]. This methodology is convenient for low-cost sensor, as the one used in our experiment. Following the methodology of of Ref. [32], we found $\tau_a = \tau_\omega = 10s$ and $\sigma_{w_f} = 0.1 m/s^2$ and $\sigma_{w_\omega} = 0.01\pi/180 rad/s$.

The last process equations are the ones related with the three Markov state vectors $\boldsymbol{\chi}_i$. Since $\boldsymbol{\chi}_i = [\boldsymbol{F}_{ai} \ \ \boldsymbol{M}_{ai} \ \ T_{A+i} \ \ T_{A-i} \ \ T_{B+i} \ \ T_{B-i} \ \ V_{wi} \ \ \psi_{wi}]$, each of these vectors has 12 components that we can denote as χ_{ij} with $i = 1 \cdots 3$ and $j = 1 \cdots 12$. The process equations can then be written in the compact form

$$\frac{d}{dt} \begin{pmatrix} \chi_{1j} \\ \chi_{2j} \\ \chi_{3j} \end{pmatrix} = \begin{pmatrix} 0 & 1 & 0 \\ 0 & 0 & 1 \\ 0 & 0 & 0 \end{pmatrix} \begin{pmatrix} \chi_{1j} \\ \chi_{2j} \\ \chi_{3j} \end{pmatrix} + \begin{pmatrix} \xi_{\chi_{1j}} \\ \xi_{\chi_{2j}} \\ \xi_{\chi_{3j}} \end{pmatrix} \tag{A23}$$

with $\xi_{\chi_{ij}}$ taken for $i = 1, 2, 3$ from normal distribution functions with zero mean and variances $\sigma_{\xi_{F_A}}^2$, $\sigma_{\xi_{M_A}}^2$, $\sigma_{\xi_T}^2$, $\sigma_{\xi_w}^2$, and $\sigma_{\xi_\psi}^2$ for $j = 1, 2, 3$, $j = 4, 5, 6$, $j = 7, 8, 9, 10$, $j = 11$ and $j = 12$, respectively.

From previous equations one readily finds the flux $\boldsymbol{f}_{proc}$, the noise vector $\boldsymbol{w}$ and matrix $\bar{\boldsymbol{G}}$ in Eq. 11. For instance, one has

$$\boldsymbol{w} = \begin{bmatrix} \boldsymbol{w}_f & \boldsymbol{w}_\omega & w_{aer} & \xi_{\chi 1,1} & \cdots & \xi_{\chi 1,12}, \end{bmatrix}$$

$$\xi_{\chi 2,1} \quad \cdots \quad \xi_{\chi 2,12}, \quad \xi_{\chi 3,1} \quad \cdots \quad \xi_{\chi 3,12} \end{bmatrix}^T \tag{A24}$$

$$\bar{\boldsymbol{G}} = \begin{bmatrix} \bar{\boldsymbol{0}}_{15 \times 43} \\ \bar{\boldsymbol{I}}_{43 \times 43} \end{bmatrix}_{58 \times 43} \tag{A25}$$

with $\bar{\boldsymbol{0}}$ a matrix with zeros and $\bar{\boldsymbol{I}}$ the identity matrix. The covariance matrix $\bar{\boldsymbol{Q}}$ has zeros everywhere except at the diagonal that reads

$$diag\left(\bar{\boldsymbol{Q}}\right) = \begin{bmatrix} \sigma_{w_f}^2 & \sigma_{w_f}^2 & \sigma_{w_f}^2 & \sigma_{w_\omega}^2 & \sigma_{w_\omega}^2 & \sigma_{w_\omega}^2 & \sigma_{w_{aer}}^2 \end{bmatrix}$$

$$\sigma_{\xi_{1,1}}^2 \cdots \sigma_{\xi_{1,12}}^2 \quad \sigma_{\xi_{2,1}}^2 \cdots \sigma_{\xi_{2,12}}^2 \quad \sigma_{\xi_{3,1}}^2 \cdots \sigma_{\xi_{3,12}}^2 \end{bmatrix} \tag{A26}$$

Table 3 summarize the parameters used in process and observation models of our EKF.

Symbol	Value	Symbol	Value
σ_{w_f}	$0.1 ms^{-2}$	σ_{w_ω}	$0.01\pi/180 rads^{-1}$
$\sigma_{w_{aer}}$	$5.0 ms^{-1}$	$\sigma_{w_{\xi_a}}$	$5.0 ms^{-2}$
σ_{ξ_m}	$15.0 Nm$	$\sigma_{v_{\xi_w}}$	$0.5 ms^{-1}$
σ_{ξ_ψ}	$\pi/180 rad$	σ_{η_r}	$5.0 m$
σ_{η_v}	$2.0 ms^{-1}$	σ_{η_a}	$0.2 ms^{-1}$
σ_{η_ω}	$4.3\pi/180 rads^{-1}$	σ_{η_B}	$0.4 G$
$\sigma_{\eta_{v_{aer}}}$	$10 ms^{-1}$	σ_{η_D}	$0.001^{-3} m$
σ_{η_T}	$10.0 N$		

Table 3: EKF Parameters

[1] Loyd, M. L., "Crosswind kite power," *Journal of Energy*, Vol. 4, No. 3, May 1980, pp. 106–111.

[2] Cherubini, A., Papini, A., Vertechy, R., and Fontana, M., "Airborne Wind Energy Systems: A review of the technologies," *Renewable and Sustainable Energy Reviews*, Vol. 51, No. Supplement C, 2015, pp. 1461 – 1476.

[3] Carpenter, H., "Tethered aircraft system for gathering energy from wind," July 3 2001, US Patent 6,254,034.

[4] Williams, P., Lansdorp, B., and Ockesl, W., "Optimal Crosswind Towing and Power Generation with Tethered Kites," *Journal of Guidance, Control, and Dynamics*, Vol. 31, No. 1, Jan 2008, pp. 81–93.

[5] Payne, P. and McCutchen, C., "Self-erecting windmill," Oct. 26 1976, US Patent 3,987,987.

[6] Felker, F., "Progress and Challenges in Airborne Wind Energy," *Book of Abstracts of the International Airborne Wind Energy Conference 2017*, edited by M. Diehl, R. Leuthold, and R. Schmehl, University of Freiburg, Delft University of Technology, Freiburg, Germany, 5–6 October 2017, p. 13, Presentation video recording available from: http://awec2017.com/presentations/fort-felker.

[7] Sánchez, G., "Dynamics and Control of Single-Line Kites," *The Aeronautical Journal*, Vol. 110, No. 1111, 2006, pp. 615Ű621.

[8] Groot, S. G. C. D., Breukels, J., Schmehl, R., and Ockels, W. J., "Modelling Kite Flight Dynamics Using a Multibody Reduction Approach," *Journal of Guidance, Control, and Dynamics*, Vol. 34, No. 6, Nov 2011, pp. 1671–1682.

[9] Gros, S. and Diehl, M., "Modeling of Airborne Wind Energy Systems in Natural Coordinates," *Airborne Wind Energy*, edited by U. Ahrens, M. Diehl, and R. Schmehl, Springer Berlin Heidelberg, Berlin, Heidelberg, 2013, pp. 181–203.

[10] Gohl, F. and Luchsinger, R. H., "Simulation Based Wing Design for Kite Power," *Airborne Wind Energy*, edited by U. Ahrens, M. Diehl, and R. Schmehl, Springer Berlin Heidelberg, Berlin, Heidelberg, 2013, pp. 325–338.

[11] Alonso-Pardo, J. and Sánchez-Arriaga, G., "Kite Model with Bridle Control for Wind-Power Generation," *Journal of Aircraft*, Vol. 52, No. 3, Apr 2015, pp. 917–923.

[12] Pastor-Rodríguez, A., Sánchez-Arriaga, G., and Sanjurjo-Rivo, M., "Modeling and Stability Analysis of Tethered Kites at High Altitudes," *Journal of Guidance, Control, and Dynamics*, Vol. 40, No. 8, May 2017, pp. 1892–1901.

[13] Salord Losantos, L. and Sánchez-Arriaga, G., "Flight Dynamics and Stability of Kites in Steady and Unsteady Wind Conditions," *Journal of Aircraft*, Vol. 52, No. 2, 2017/05/10 2014, pp. 660–666.

[14] Sánchez-Arriaga, G., García-Villalba, M., and Schmehl, R., "Modeling and dynamics of a two-line kite," *Applied Mathematical Modelling*, Vol. 47, 2017, pp. 473 – 486.

[15] Bosch, A., Schmehl, R., Tiso, P., and Rixen, D., "Dynamic Nonlinear Aeroelastic Model of a Kite for Power Generation," *Journal of Guidance, Control, and Dynamics*, Vol. 37, No. 5, Jun 2014, pp. 1426–1436.

[16] Folkersma, M., Schmehl, R., and Viré, A., "Fluid-Structure Interaction Simulations on Kites," *Book of Abstracts of the International Airborne Wind Energy Conference 2017*, edited by M. Diehl, R. Leuthold,

and R. Schmehl, Freiburg, Germany, 2017, pp. 1–188.

[17] de Wachter, A., *Deformation and Aerodynamic Performance of a Ram-Air Wing*, Msc thesis, Delft University of Technology, 2008.

[18] Milne, G., Soijer, M., Juliana, S., Hermansyah, M., and Mulder, J., *Maximum likelihood stability and control derivative identification of a Cessna Citation II*, American Institute of Aeronautics and Astronautics, 2017/11/13 2001.

[19] Piotr, L. and Maciej, L., *meceng*, Vol. 60, chap. Maximum Likelihood Estimation for Identification of Aircraft Aerodynamic Derivatives, 2018 2013, p. 219, 2.

[20] Ramachandran, S., Schneider, H., Mason, J., and Stalford, H., chap. Identification of aircraft aerodynamic characteristics at high angles of attack and sideslip using the estimation before modeling /EBM/ technique, Guidance, Navigation, and Control and Co-located Conferences, American Institute of Aeronautics and Astronautics, Aug 1977.

[21] Hoff, J. C. and Cook, M. V., "Aircraft parameter identification using an estimation-before-modelling technique," *The Aeronautical Journal (1968)*, Vol. 100, No. 997, 009 1996, pp. 259–268.

[22] Mulder, J., Chu, Q., Sridhar, J., Breeman, J., and Laban, M., "Non-linear aircraft flight path reconstruction review and new advances," *Progress in Aerospace Sciences*, Vol. 35, 10 1999, pp. 673–726.

[23] *Optimum Experimental Design of a Rigid Wing AWE Pumping System*, 2017.

[24] Licitra, G., Bürger, A., Williams, P., Ruiterkamp, R., and Diehl, M., "System Identification of a Rigid Wing Airborne Wind Energy System," *submitted*.

[25] Hummel, J., *Automatisierte Vermessung und Charakterisierung der dynamischen Eigenschaften seilgebundener, vollflexibler Tragflachen*, PhD dissertation, Berlin University of Technology, 2017.

[26] Oehler, J. and Schmehl, R., "Experimental Characterization of a Force-Controlled Flexible Wing Traction Kite," *Book of Abstracts of the International Airborne Wind Energy Conference 2017*, edited by M. Diehl, R. Leuthold, and R. Schmehl, Albert Ludwig University Freiburg and Delft University of Technology, Freiuburg, Germany, 2017, pp. 1–188.

[27] Fagiano, L., Huynh, K., Bamieh, B., and Khammash, M., "On Sensor Fusion for Airborne Wind Energy Systems," *IEEE Transactions on Control Systems Technology*, Vol. 22, No. 3, May 2014, pp. 930–943.

[28] Fagiano, L., Zgraggen, A. U., Morari, M., and Khammash, M., "Automatic Crosswind Flight of Tethered Wings for Airborne Wind Energy: Modeling, Control Design, and Experimental Results," *IEEE Transactions on Control Systems Technology*, Vol. 22, No. 4, July 2014, pp. 1433–1447.

[29] Sri-Jayantha, M. and Stengel, R. F., "Determination of nonlinear aerodynamic coefficients using the estimation-before-modeling method," *Journal of Aircraft*, Vol. 25, No. 9, Sep 1988, pp. 796–804.

[30] Goszczyński, J. A., Michalski, W. J., and Pietrucha, J. A., "Estimation before modelling as the method for identification of the aircraft aerodynamic characteristics in nonlinear flight regime," *Journal of Theoretical and Applied Mechanics*, Vol. 38, No. 1, 2000.

[31] Welch, G. and Bishop, G., "An Introduction to the Kalman Filter," Tech. rep., Chapel Hill, NC, USA, 1995.

[32] Xing, Z. and Gebre-Egziabher, D., "Modeling and bounding low cost inertial sensor errors," *2008 IEEE/ION Position, Location and Navigation Symposium*, Monterey, CA, USA, May 2008, pp. 1122–1132.